

MODEL REDUCTION WITH MAPREDUCE-ENABLED TALL AND SKINNY SINGULAR VALUE DECOMPOSITION

PAUL G. CONSTANTINE*, DAVID F. GLEICH†, YANGYANG HOU‡, AND JEREMY TEMPLETON§

Abstract. We present a non-intrusive method for computing reduced order models of parameterized partial differential equation solutions. The key analytical tool is the singular value expansion of the parameterized solution, which we approximate via a singular value decomposition of a matrix whose columns are solutions of the PDE model at different values of the parameter. To evaluate a new solution, we interpolate a subset of the right singular vectors to estimate the coefficients in the singular value expansion evaluated at a new parameter. We employ a novel method to select this subset that uses the parameter gradient of the right singular vectors to split the terms in the expansion yielding a mean prediction and a prediction covariance—similar to a Gaussian process approximation.

We demonstrate the efficacy of the reduced order model using an uncertainty quantification study of heat transfer in random media. The high fidelity simulations produce more than 4TB of data; we compute the singular value decomposition and evaluate the reduced order model using scalable MapReduce/Hadoop implementations. We compare the accuracy of our method to a scalar response surface on a set of temperature profile measurements and find that our model better captures sharp, local features in the parameter space.

Key words. model reduction, simulation informatics, MapReduce, Hadoop, tall and skinny SVD

1. Introduction & motivation. When high-fidelity simulations of parameterized partial differential equations are prohibitively expensive, cheaper reduced order models (ROMs) can be used in parameter studies like optimization and uncertainty quantification, where many independent runs are necessary. Often the reduced order models are trained on a relatively small set of high-fidelity runs that are chosen to cover a range of input parameter values; reduced basis methods [4, 7, 20] and collocation-based methods [1, 23] operate in such a manner. Reduced basis methods provide a measure of confidence in the reduced order model, but they often require modifications to existing high-fidelity solvers. In contrast, the *non-intrusive* collocation methods commonly used in uncertainty quantification can use existing solvers, but error estimates are more difficult to compute.

We propose a non-intrusive method for model reduction for parameterized partial differential equations (PDEs) that comes equipped with a measure of confidence. The method is based on the singular value expansion (SVE) of the parameterized solution, which we approximate by the singular value decomposition (SVD) of a tall, dense matrix of PDE solutions computed at a set of input parameter values. The SVD step compares to the basis computation in reduced basis methods, where the ROM is a linear combination of a subset of the left singular vectors. But instead of a subsequent projection step to create a small system whose solution yields the coefficients of the linear combination, we compute the coefficients by interpolating the right singular vectors in the parameter domain. For each parameter value where we wish to evaluate

*Stanford University, Stanford, California 94305 (paul.constantine@stanford.edu).

†Purdue CS, West Lafayette, Indiana 47907 (dgleich@purdue.edu).

‡Purdue CS, West Lafayette, Indiana 47907 (houl3@purdue.edu).

§Sandia National Laboratories, Livermore, California (jatempl@sandia.gov). Sandia National Laboratories is a multi-program laboratory managed and operated by Sandia Corporation, a wholly owned subsidiary of Lockheed Martin Corporation, for the U.S. Department of Energy's National Nuclear Security Administration under contract DE-AC04-94AL85000.

the reduced model, the right singular vectors are divided into two categories: (i) those that are sufficiently smooth to be accurately interpolated, and (ii) those that have too many oscillations (i.e., zero-crossings) for accurate interpolation. The latter category identifies a subset of the reduced basis that can be used to compute a prediction variance in a manner similar to Gaussian process models for interpolation [19]. The heuristics we employ to categorize the singular vectors are based on the work of Hansen in the context of ill-posed inverse problems [12].

For large computational models with many degrees of freedom, computing the SVD is expensive and data-intensive. Special algorithms may be necessary when the data matrix does not fit into main memory. In this paper, we utilize a *communication-avoiding* SVD [9] for the tall, skinny data matrix of PDE solutions. The factorization algorithm is implemented in the Hadoop distribution [5] of MapReduce [8], as described in our previous work [6]; we briefly review this implementation in Section 3. This implementation enables us to compute the SVD of a matrix with five billion rows and sixty-four columns, which contains approximately 2.2 terabytes of data. In Section 3 we describe how the matrix is derived and how its SVD components are used to construct the reduced order model.

We apply the model reduction method with the tall, skinny SVD to three-dimensional, time-dependent heat transfer problem in random media. An object is heated on one side, and the objective is to study how much heat transfers to the opposite side given the parameterized thermal conductivity of the material. The high-fidelity simulations use Sandia National Laboratories' finite element production code Aria [17] on its capacity cluster with a mesh containing 4.2M elements. The reduced order model is constructed and evaluated on a ten-node Hadoop cluster. In Section 4, we study the effectiveness of the reduced order model and compare its predictions to a cubic spline response surface on two relevant scalar quantities of interest computed from the full temperature distribution.

2. A reduced order modeling approach. Let $f = f(x, s)$ be the solution of a partial differential equation (PDE), where $x \in \mathcal{X} \subset \mathbb{R}^4$ are the space and time coordinates (three spatial dimensions and a temporal dimension), and $s \in \mathcal{S} \subset \mathbb{R}$ is an input parameter. The origin of f is important because computational tools will compute f at all values of x given an input s . In other words, we cannot evaluate f at a specific x without evaluating it for every x .

We assume that computing $f(x, s)$ for a particular s is computationally expensive. The number N of solutions we may compute is constrained by a budget. More precisely, for $s_j \in \mathcal{S}$ with $j = 1, \dots, N$, assume we have $f_j = f(x, s_j)$. We want to use the f_j to construct an approximation—i.e., a reduced order model—of $f(x, s)$ for $s \neq s_j$ that is less computationally expensive than solving the differential equation. We can then use the reduced order model for further parameter studies.

We restrict our attention to models with a single scalar parameter. This is mostly for practical purposes. In the following sections, we will employ interpolation operators and compute approximations of the derivative in the parameter space \mathcal{S} . While these operations can in principle be extended to models with multiple parameters, challenges arise in higher dimensions that, for the sake of focus and simplicity, we will avoid in this manuscript.

We assume that f is continuous and square-integrable, i.e.,

$$\int_{\mathcal{X}} \int_{\mathcal{S}} f^2 ds dx < \infty, \quad (2.1)$$

which will permit us to use the singular value expansion. In practice, the techniques we use perform better if f is smooth, e.g., admits continuous derivatives up to some order. We will rely heavily on Hansen's work [10, 11, 13, 12], which analyzes the singular value expansion of an integral equation kernel and its discrete counterpart, the singular value decomposition, in the context of discrete, ill-posed inverse problems.

2.1. Singular value expansion. Since we assume f is continuous, it admits a uniformly convergent series representation known as the *singular value expansion* (SVE); see [10] for more details on the SVE:

$$f(x, s) = \sum_{k=1}^{\infty} \mu_k u_k(x) v_k(s). \quad (2.2)$$

The singular functions $u_k(x)$ and $v_k(s)$ are continuous and orthonormal, i.e.,

$$\int_{\mathcal{X}} u_{k_1} u_{k_2} dx = \int_{\mathcal{S}} v_{k_1} v_{k_2} ds = \delta_{k_1, k_2}. \quad (2.3)$$

The singular values are positive and ordered in decreasing order,

$$\mu_1 \geq \mu_2 \geq \dots \geq 0. \quad (2.4)$$

If only finitely many μ_k are non-zero, then f is *degenerate*.

Hansen has observed [13, 12] that, for a broad class of integral equation kernels found in practice, the singular functions become more oscillatory (i.e., cross zero more frequently) as the index k increases. Rigorous proofs of this observation are available for some special cases, but it is easy to construct functions whose singular functions do not behave this way.

We have also observed this phenomenon for functions $f = f(x, s)$ coming from parameterized partial differential equations, and it is corroborated by many studies in coherent structures based on the closely related proper orthogonal decomposition [15]. Additionally we have observed that these oscillations increase more rapidly in regions where f has large gradients. For example, if $f(x, s)$ is the solution of an advection-diffusion equation with s being the Peclet number (i.e., ratio of advection to diffusion), then the singular functions $v_k(s)$ will oscillate more rapidly in regions of large s corresponding to advection dominated solutions. We will show another example of this phenomenon in Section 2.5, and we will exploit this observation when constructing the reduced order model.

2.2. Approximating the SVE with the SVD. Hansen discusses methods for approximating the factors of the singular value expansion using the singular value decomposition. We will implicitly employ his construction from [10, Section 5], which ultimately uses point evaluations of the function f to construct a matrix suitable for the SVD.

Let x_1, \dots, x_M with $x_i \in \mathcal{X}$ be the points of a discretization of the spatio-temporal domain. A run of the PDE solver produces an approximate solution at these points in the domain for a given input s . We assume that the spatio-temporal discretization is sufficient to produce an accurate approximation of the PDE solution for all values of s ; in practice, such an assumption should be verified. Let s_1, \dots, s_N with $s_j \in \mathcal{S}$ be a set of input parameters where the approximate PDE solution will be computed. For simplicity, we will assume that \mathcal{S} is a closed interval with a uniform discretization

$$\mathcal{S} = [s_1, s_N], \quad s_j = s_1 + (j-1)\Delta s, \quad \Delta s = \frac{s_N - s_1}{N-1}. \quad (2.5)$$

The number N is the budget of simulations, and we expect that $N \ll M$ for most cases. In other words, we assume that the number of nodes in the spatio-temporal discretization is much larger than the budget of simulations.

From these approximate solutions, we construct the tall, dense matrix

$$\mathbf{F} = \begin{bmatrix} f(x_1, s_1) & \cdots & f(x_1, s_N) \\ \vdots & \ddots & \vdots \\ f(x_M, s_1) & \cdots & f(x_M, s_N) \end{bmatrix}. \quad (2.6)$$

Next we compute the thin SVD

$$\mathbf{F} = \mathbf{U}\Sigma\mathbf{V}^T, \quad \Sigma = \text{diag}(\sigma_1, \dots, \sigma_N), \quad (2.7)$$

where, following [10], we treat $\sigma_k \approx \mu_k$ and

$$\mathbf{U} \approx \begin{bmatrix} u_1(x_1) & \cdots & u_N(x_1) \\ \vdots & \ddots & \vdots \\ u_1(x_M) & \cdots & u_N(x_M) \end{bmatrix}, \quad \mathbf{V} \approx \begin{bmatrix} v_1(s_1) & \cdots & v_N(s_1) \\ \vdots & \ddots & \vdots \\ v_1(s_N) & \cdots & v_N(s_N) \end{bmatrix} \quad (2.8)$$

The components of the singular vectors inherit the observed oscillating behavior of the singular functions. In particular, the oscillations increase as the index k increases, and they increase more rapidly in regions corresponding to large differences in the elements of the data matrix \mathbf{F} .

These rapid oscillations manifest as an increase in the magnitude of the difference between neighboring components of the singular vectors as k increases¹. However, in this case of finite resolution, there is typically some k after which the discretization is insufficient to represent the oscillations. The phenomenon is similar to approximating a sequence of sine waves with increasing frequency using the same grid. We formalize this notion in the following assumption.

ASSUMPTION 1. *There is an $R \leq N$ such that the sequence of difference magnitudes between neighboring singular vector components will increase for k from 1 to R ,*

$$|v_{k+1}(s_{i+1}) - v_{k+1}(s_i)| > |v_k(s_{i+1}) - v_k(s_i)|. \quad (2.9)$$

For $k > R$, the relationship becomes unpredictable due to the finite resolution in s .

We will use Assumption 1 to justify a heuristic that distinguishes between singular functions that can be resolved and those that cannot given the discretization.

2.3. Constructing the reduced order model. Recall that the goal is to approximate $f(x, s)$ for some input s that was not used to compute a training run. We can use the existence of the SVE to justify the following approach. Since we treat the components of the right singular vectors \mathbf{V} as evaluations of the singular functions $v_k(s)$, we can interpolate between the singular vector components to approximate the singular functions at new values of s . More precisely, define

$$\tilde{v}_k(s) = \mathcal{I}(s; v_k(s_1), \dots, v_k(s_N)) \quad (2.10)$$

where \mathcal{I} is an interpolation operator that takes a value of s and the components of the singular vector as arguments. The form of the interpolant may depend on the

¹When the model contains more than one parameter, the notion of *neighboring components* becomes more complicated.

selection of the points s_j . For example, if these points are the Chebyshev points or the nodes of a Gaussian quadrature rule, then high order global polynomial interpolation is possible. If the points are uniformly spaced, then one may use piecewise polynomials or radial basis functions. In the numerical examples that follow, we will use cubic splines.

Unfortunately, the increasingly oscillatory character of the functions $v_k(s)$ as k increases combined with the fixed discretization s_j causes concern for any chosen interpolation procedure as k approaches N . In other words, the smoothness of $v_k(s)$ decreases as k increases, which diminishes confidence in the interpolation accuracy.

Therefore, we seek to split the interpolations into two groups: *trusted* and *untrusted*. More specifically, we seek an $R = R(s)$ with $R \leq N$ such that for $k \leq R$ we have confidence in the accuracy of the interpolant $\tilde{v}_k(s)$. We treat the remaining interpolations with $k > R$ as unpredictable, and we model them with a standard normal random variable. The choice of the standard normal distribution is justified by the orthonormality of the singular vectors. We will discuss the choice of R in the next section.

Given R , we model the PDE output at the space-time coordinate x_i for the new parameter value s as

$$\tilde{f}(x_i, s) = \sum_{k=1}^R \sigma_k u_k(x_i) \tilde{v}_k(s) + \sum_{k=R+1}^N \sigma_k u_k(x_i) \eta_{k-R}, \quad (2.11)$$

where $\eta_k \sim N(0, 1)$ are i.i.d. and represent the uncertainty in the interpolation procedure for increasingly oscillatory functions. Under this construction, the vector of values $f(x_i, s)$ has a multivariate Gaussian distribution with mean and covariance given by

$$\begin{aligned} \mathbb{E} [\tilde{f}(x_i, s)] &= \sum_{k=1}^R \sigma_k u_k(x_i) \tilde{v}_k(s) \\ \text{Cov} [\tilde{f}(x_i, s), \tilde{f}(x_j, s)] &= \sum_{k=R+1}^N \sigma_k^2 u_k(x_i) u_k(x_j). \end{aligned} \quad (2.12)$$

The reduced order model we propose is the mean of this Gaussian random vector,

$$f(x_i, s) \approx \mathbb{E} [\tilde{f}(x_i, s)]. \quad (2.13)$$

The diagonal components of the covariance matrix provide a measure of confidence for the reduced order model at each x_i similar to the prediction variance of a Gaussian process regression model [19].

Next we show the reduced order model is equivalent to applying the interpolation procedure independently to the rows of a low rank approximation of the matrix \mathbf{F} . To set up the notation, partition

$$\mathbf{U} = [\mathbf{U}_1 \quad \mathbf{U}_2], \quad \Sigma = \begin{bmatrix} \Sigma_1 & \\ & \Sigma_2 \end{bmatrix}, \quad \mathbf{V} = [\mathbf{V}_1 \quad \mathbf{V}_2], \quad (2.14)$$

where \mathbf{U}_1 , Σ_1 , and \mathbf{V}_1 contain R columns. Then

$$\begin{aligned}
\mathbf{F} &= \mathbf{U}\Sigma\mathbf{V}^T \\
&= \mathbf{U}_1\Sigma_1\mathbf{V}_1^T + \mathbf{U}_2\Sigma_2\mathbf{V}_2^T \\
&= \mathbf{F}_1 + \mathbf{F}_2 \\
&= \begin{bmatrix} f^{(1)}(x_1, s_1) & \cdots & f^{(1)}(x_1, s_N) \\ \vdots & \ddots & \vdots \\ f^{(1)}(x_M, s_1) & \cdots & f^{(1)}(x_M, s_N) \end{bmatrix} + \begin{bmatrix} f^{(2)}(x_1, s_1) & \cdots & f^{(2)}(x_1, s_N) \\ \vdots & \ddots & \vdots \\ f^{(2)}(x_M, s_1) & \cdots & f^{(2)}(x_M, s_N) \end{bmatrix}.
\end{aligned} \tag{2.15}$$

Then we have the following theorem.

THEOREM 2.1. *If \mathcal{I} from (2.10) is a linear operation, then*

$$\begin{aligned}
\mathbb{E} \left[\tilde{f}(x_i, s) \right] &= \mathcal{I} \left(s; f^{(1)}(x_i, s_1), \dots, f^{(1)}(x_i, s_N) \right), \\
\text{Cov} \left[\tilde{f}(x_i, s), \tilde{f}(x_j, s) \right] &= \sum_{k=R+1}^N f^{(2)}(x_i, s_k) f^{(2)}(x_j, s_k).
\end{aligned} \tag{2.16}$$

Proof. For a function $g = g(s)$ with evaluations $g(s_j)$ the linear interpolation can be written

$$\mathcal{I}(s; g(s_1), \dots, g(s_N)) = \sum_{j=1}^N w_j g(s_j) \tag{2.17}$$

for some set of weights $w_j = w_j(s)$. Then,

$$\begin{aligned}
\mathbb{E} \left[\tilde{f}(x_i, s) \right] &= \sum_{k=1}^R \sigma_k u_k(x_i) \tilde{v}_k(s) \\
&= \sum_{k=1}^R \sigma_k u_k(x_i) \left(\sum_{j=1}^N w_j v_k(s_j) \right) \\
&= \sum_{j=1}^N w_j \left(\sum_{k=1}^R \sigma_k u_k(x_i) v_k(s_j) \right) \\
&= \sum_{j=1}^N w_j f^{(1)}(x_i, s_j) \\
&= \mathcal{I} \left(s; f^{(1)}(x_i, s_1), \dots, f^{(1)}(x_i, s_N) \right),
\end{aligned} \tag{2.18}$$

as required. The covariance expression is easily proved using the linear algebra notation. Define the $N \times N$ matrix $\mathbf{C}_{ij} = \text{Cov} \left[\tilde{f}(x_i, s), \tilde{f}(x_j, s) \right]$. Then by the orthogonality of the columns of \mathbf{V}_2 ,

$$\mathbf{C} = \mathbf{U}_2\Sigma_2^2\mathbf{U}_2^T = \mathbf{U}_2\Sigma_2\mathbf{V}_2^T\mathbf{V}_2\Sigma_2^T\mathbf{U}_2^T = \mathbf{F}_2\mathbf{F}_2^T. \tag{2.19}$$

as required. \square

2.4. Choosing R . We must still choose R that determines the split between trusted and untrusted interpolations on the elements of \mathbf{V} . We will make use of Assumption 1 and define the following *variation metric*,

$$\tau(r, s) = \sum_{k=1}^r \left| \frac{v_k(s_{j+1}) - v_k(s_j)}{\Delta s} \right|, \quad \text{for } s_j \leq s < s_{j+1}. \quad (2.20)$$

By Assumption 1, τ is an increasing function of r up to some $R = R(s)$. Loosely, if τ is too large, then we have entered the range of k where interpolations of $v_k(s_j)$ are not to be trusted. We will quantify this with a threshold $\bar{\tau}$. Given $\bar{\tau}$, we choose $R = R(s, \bar{\tau})$ to be the largest r such that $\tau(r, s) \leq \bar{\tau}$.

To determine the appropriate threshold $\bar{\tau}$, we use a set of PDE evaluations $f_\ell = f(x, s_\ell)$ with $\ell = 1, \dots, L$ for testing, where s_ℓ is not in the training set. For the testing models, we compute the error

$$\mathcal{E}(s_\ell, \bar{\tau}) = \left[\sum_{i=1}^M \left(f(x_i, s_\ell) - \sum_{k=1}^R \sigma_k u_k(x_i) \tilde{v}_k(s_\ell) \right)^2 / \sum_{i=1}^M f(x_i, s_\ell)^2 \right]^{1/2} \quad (2.21)$$

for some set of thresholds $\bar{\tau}$, where $R = R(s_\ell, \bar{\tau})$. These errors can be visualized, and the threshold is chosen so that the error in the testing set is relatively small. We will demonstrate this on a simple example in the next section.

We can compare the splitting strategy based on $R = R(s)$ to a standard truncation strategy based on the magnitudes of the singular values of \mathbf{F} . The mean of the Gaussian process approximation (2.13) is equivalent to interpolating a truncated SVD approximation of the data matrix \mathbf{F} , as shown in Theorem 2.1. However, the magnitudes of the singular values provide no insight into the uncertainty in the interpolation procedure. The splitting strategy chooses a different truncation for the mean (2.13) for each s based on the capability of the interpolation procedure to accurately approximate the singular functions $v_k(s)$ at the point s . The singular values that are not in the mean contribute to the prediction variance. A global truncation based on the singular values would create the same prediction variance for every s , and it would always be on the order of the largest truncated singular value. In other words, it provides no information on how the confidence in the prediction changes as s varies.

2.5. A numerical example. Consider the boundary value problem

$$-\frac{d}{dx} \left(a \frac{df}{dx} \right) = 1, \quad x \in [0, 1], \quad (2.22)$$

with coefficients

$$a = a(x, s) = 1 + 4s(x^2 - x), \quad s \in [0.1, 0.9], \quad (2.23)$$

and boundary conditions $f(x = 0, s) = f(x = 1, s) = 0$. The solution is

$$f(x, s) = -\frac{1}{8s} \log(1 + 4s(x^2 - x)), \quad (2.24)$$

which is plotted in Figure 2.1. Outside the domain, f has a singularity at $(x = 0.5, s = 1)$, which causes f to grow rapidly along the line $x = 0.5$ near the boundary $s = 0.9$. This local feature of the solution results in more rapid oscillations of the

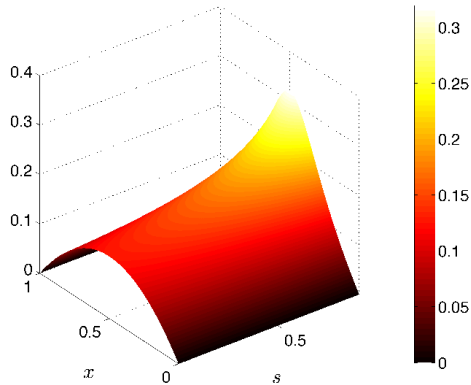


Fig. 2.1: A surface of the function $f(x, s)$ from 2.24. Notice the rapid growth near the point $(x = 0.5, s = 0.9)$. (Colors are visible in the electronic version.)

singular functions $v_k(s)$ near the boundary $s = 0.9$. The first eight singular functions, scaled by the singular values, are plotted in Figure 2.2. The rapid oscillations near the parameter boundary $s = 0.9$ are clearly visible.

In those same figures, we plot the components of the corresponding singular vectors, scaled by the singular values, for a data matrix \mathbf{F} with columns computed at eleven equally spaced parameter values in the interval $[0.1, 0.9]$; we will build the reduced order model from this data matrix with these eleven training models. Notice how the components of the singular vectors deviate from the singular functions as k increases, particularly in the regions of rapid oscillations.

We compute a test model at each midpoint of intervals $[s_i, s_{i+1}]$, where s_i was used to compute the training models. The range of the variation metric τ from (2.20) for these testing sites is roughly 0.1 to 42.8. We choose twenty candidate thresholds $\bar{\tau}$ in this range and compute the error in the reduced order model at the testing sites (see (2.21)) for each candidate threshold. These errors are displayed in Figure 2.3. It is clear from the figure that the reduced order model is optimally accurate for each testing site after the fourth candidate threshold, which is roughly $\bar{\tau} = 6.84$. For this threshold, Table 2.1 displays the split R between the bases that admit a trusted interpolant and those that are modeled with a random variable for each of the testing sites. Notice that the number of trusted bases is smaller for testing sites near the boundary $s = 0.9$ of the parameter domain, which is precisely what we would have expected.

3. Implementation in Hadoop. Constructing the ROM for highly resolved simulations (i.e., large M) requires significant data processing. We have implemented the construction in the MapReduce framework, which enables us to take advantage of Hadoop for large-scale distributed data processing. In this section, we describe the implementation including a brief review of MapReduce and Hadoop.

3.1. MapReduce/Hadoop. Google devised MapReduce because of the frustration programmers experienced as they constantly juggled the complexity of developing distributed, fault-tolerant data computational algorithms [8]. Early data-intensive computing at Google was a complex mix of ad hoc scripts. Their solution was the

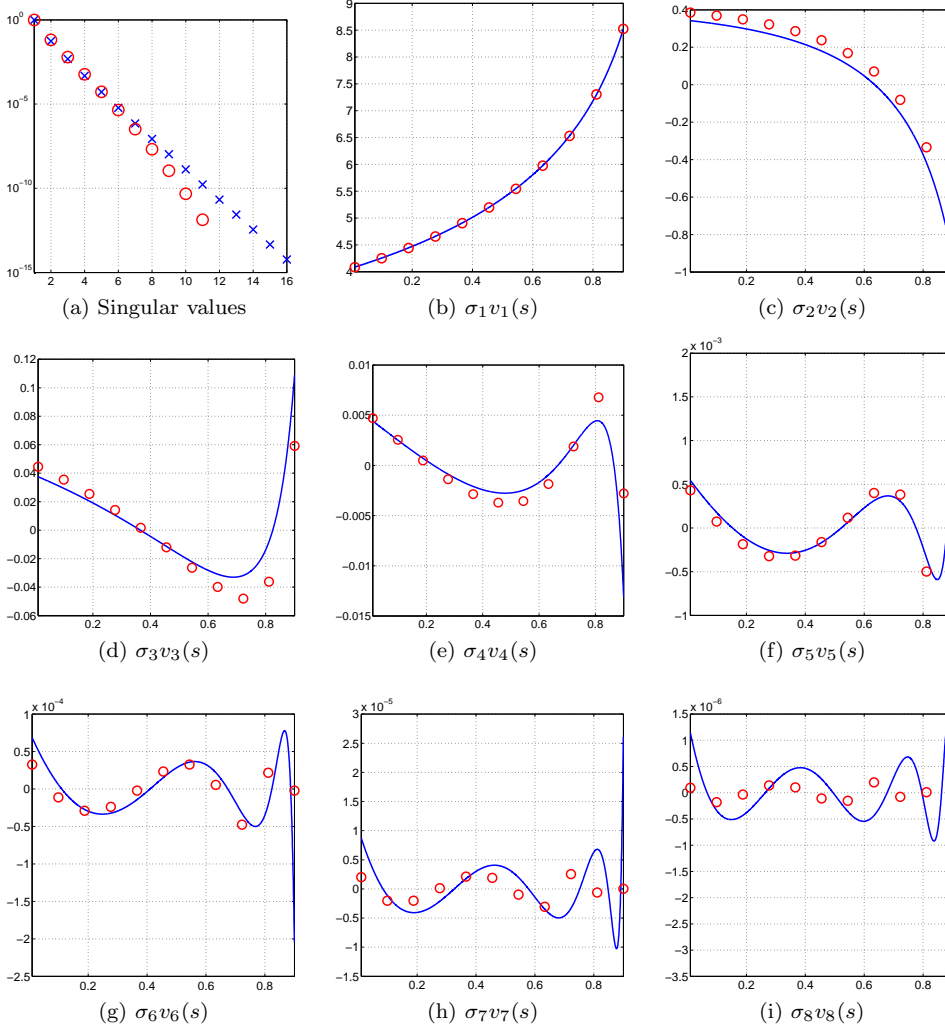


Fig. 2.2: The top left figure shows the singular values of a finely resolved \mathbf{F} with 1001 columns (blue x's) and a coarsely resolved \mathbf{F} with 11 columns (red o's). Each are scaled by the maximum singular value from each set. The remaining figures show the approximations of the singular functions $v_1(s)$ through $v_8(s)$ scaled by the respective singular values for \mathbf{F} with 1001 columns (blue lines) and 16 columns (red o's). (Colors are visible in the electronic version.)

MapReduce computation model: a simple, general interface for a common template behind their data analysis tasks that hides the details of the parallel implementations from the programmer. Due to its generality, the MapReduce computation model has also been an effective paradigm for parallelizing tasks on GPUs [14], multi-core systems [21], and traditional HPC clusters [18].

The MapReduce model consists of two elements inspired by functional programming: a *map* operation to transform the input into a key/value pair and a *reduce* operation to process information with the same key. The user provides both func-

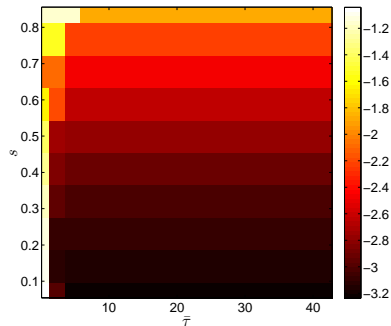


Fig. 2.3: The log of the relative error in the mean prediction of the ROM as a function of s and $\bar{\tau}$. (Colors are visible in the electronic version.)

s	$R(s, \bar{\tau})$	$\mathcal{E}(s, \bar{\tau})$
0.0545	4	0.0006
0.1435	5	0.0007
0.2325	6	0.0008
0.3215	6	0.0010
0.4105	5	0.0013
0.4995	6	0.0017
0.5885	4	0.0023
0.6775	5	0.0034
0.7665	3	0.0059
0.8555	2	0.0129

Table 2.1: The split and the corresponding ROM error for $\bar{\tau} = 6.84$ and different values of s .

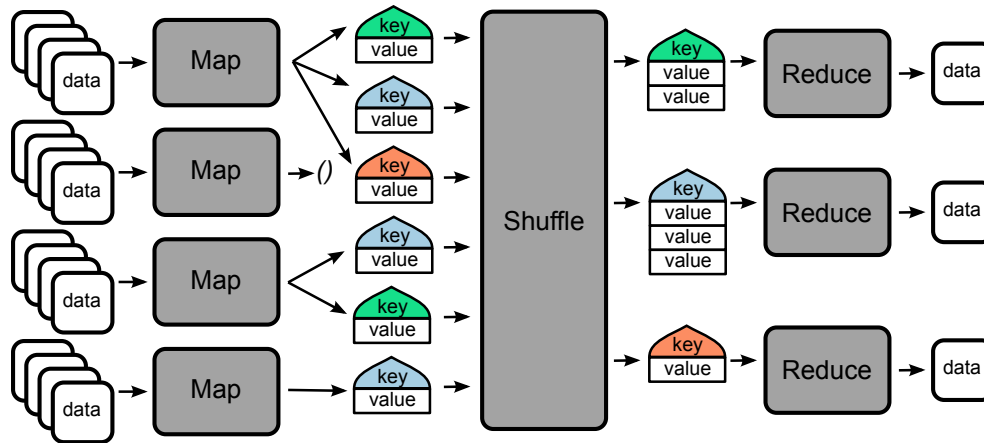


Fig. 3.1: The MapReduce system by Google is inspired by a functional programming paradigm and consists of three phases that transform data (*map*), aggregate results (*shuffle*), and compute and store (*reduce*). All Map and Reduce functions are independent, which allows the system to schedule them in parallel.

tions, which cannot have any side effects. A MapReduce implementation executes the *map* function on the entire dataset in parallel, as in Figure 3.1. A canonical MapReduce dataset is a terabyte-sized, text file split into individual lines. In this case, each *map* function receives only a few thousand lines from the enormous file, which it processes and sends via *shuffle* to the appropriate *reduce* function. The *shuffle* operation groups *map* outputs by the key, and the *reduce* function processes all outputs with the same key—e.g., counting the number of times a word appears in a large document.

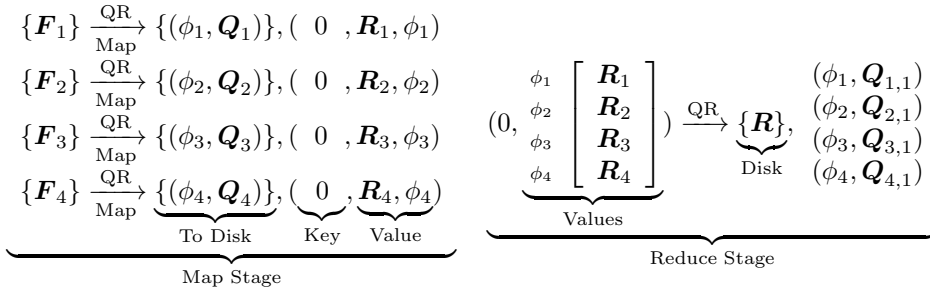
Google’s implementation of MapReduce is proprietary. An alternative, open source implementation named Hadoop has become the industry standard for large-scale data processing. More information on Hadoop can be found at the Cloudera website [22].

3.2. Model reduction in MapReduce. To construct the reduced order model, the outputs from the high-fidelity simulations are sent to and stored in the Hadoop cluster. Our implementation then proceeds in three steps:

1. Create the tall-and-skinny matrix \mathbf{F} from the simulation data.
2. Compute the singular value decomposition of \mathbf{F} (Section 3.3).
3. Generate the coefficients of the reduced-order model and evaluate solutions from the ROM (Section 3.4).

The first step is to reorganize the data into the tall-and-skinny matrix \mathbf{F} . This step is particularly communication intensive as it requires reorganizing the data from the columns (the natural outputs of the simulations) to rows for the tall-and-skinny SVD routine. To do this in Hadoop we create a text file where each line is a path to a file containing the outputs of one simulation (i.e., a column of \mathbf{F}). Then the *map* function reads a simulation from the file system and outputs the data keyed on the row of matrix \mathbf{F} . The *reduce* function aggregates all the entries in the row and outputs the realized row. The outcome of this first MapReduce iteration is the matrix \mathbf{F} stored by rows on the distributed file system.

3.3. TSQR and SVD in Hadoop. Once we have the matrix \mathbf{F} stored by rows on disk, we can compute a tall-and-skinny QR (TSQR) factorization of the matrix \mathbf{F} [2]. The basis for the MapReduce TSQR algorithm is the communication-avoiding QR factorization [9]. The strategy is to divide the tall-and-skinny matrix \mathbf{F} into many smaller, tall matrices to be decomposed independently via the QR factorization. This process is repeated on the new matrix formed by all the \mathbf{R} factors computed in the previous step until there is only a single \mathbf{R} left. This algorithm was shown to have superior numerical stability to a large Householder-style procedure [16]. The Hadoop Distributed File System stores the matrix in small chunks according to its internal splitting procedure. Each *map* function reads a small local matrix and computes a QR factorization. It then writes the \mathbf{Q} factor back to disk with a small tag ϕ . Finally, it outputs the \mathbf{R} factor and the same tag ϕ with the same key so that one reducer receives all the partial factors \mathbf{R}_ϕ . The following figure demonstrates the procedure when \mathbf{F} is split into four blocks.



There are two types of outputs represented: (i) those with $\{\dots\}$ are written to disk for processing in the future and (ii) those with (\dots) are used in the next stage. The tag ϕ_i is a random string of data created to uniquely tag each *map* function. To get the left singular vectors \mathbf{U} from the QR factors, we compute the SVD of the matrix $\mathbf{R} = \mathbf{U}_R \mathbf{\Sigma} \mathbf{V}^T$ and store $\mathbf{\Sigma}$ and \mathbf{V} on disk.² With another *reduce*, we distribute the matrix \mathbf{U}_R to all reducers. Then we aggregate all outputs with the same tag ϕ_i and

²Note that the size of \mathbf{R} is $N \times N$, where N is the number of high fidelity simulations; we assume that N is at most on the order of thousands.

compute the products $\mathbf{Q}_i \mathbf{Q}_{i,1} \mathbf{U}_R$. This is a numerically stable computation of \mathbf{U} in the SVD of \mathbf{F} stored on the distributed file system. The codes for computing the TSQR and TSSVD can be found at github.com/dgleich/mrtsqr.

3.4. Evaluating the reduced order model in MapReduce. Next we describe the procedure for evaluating the ROM in MapReduce for a given parameter value s . If one needs to evaluate the ROM at many values of s , this can be done in parallel with our existing codes.

There are two steps involved in evaluating the ROM. The first step is evaluating the interpolated function $\tilde{v}_k(s)$ at s . Since \mathbf{V} and Σ are small, this step is easily executed on a single machine. The second step is estimating the ROM prediction and its variance via

$$\mathbb{E} [\tilde{f}(x_i, s)] = \sum_{k=1}^R u_k(x_i) \sigma_k \tilde{v}_k(s), \quad \text{Var} [\tilde{f}(x_i, s)] = \sum_{k=R+1}^N \sigma_k^2 u_k(x_i)^2. \quad (3.1)$$

Recall that $R = R(s)$ is the splitting of the singular value expansion at the point s described in 2.4. Further, recall, that the matrix \mathbf{U} computed in the SVD of \mathbf{F} holds the coefficients $u_k(x_i)$. We can evaluate the ROM at all points x_i by computing the matrix-vector product:

$$\mathbf{f}(s) = \mathbf{U}(:, 1 : R) \tilde{\mathbf{v}}(s), \quad (3.2)$$

where

$$\mathbf{f}(s) = \begin{bmatrix} \mathbb{E} [\tilde{f}(x_1, s)] \\ \vdots \\ \mathbb{E} [\tilde{f}(x_M, s)] \end{bmatrix}, \quad \tilde{\mathbf{v}}(s) = \begin{bmatrix} \sigma_1 \tilde{v}_1(s) \\ \vdots \\ \sigma_1 \tilde{v}_R(s) \end{bmatrix}. \quad (3.3)$$

Since the matrix \mathbf{F} , and hence \mathbf{U} , is tall-and-skinny, we can compute such matrix-vector products in Hadoop by distributing the small vector $\tilde{\mathbf{v}}$ to a *map* function that will compute a portion of the matrix-vector product. A subsequent *reduce* collects each submatrix-vector product into a single file. Viewed schematically for \mathbf{U} stored in four blocks,

$$\underbrace{\begin{array}{l} \{\mathbf{U}_1\} \\ \{\mathbf{U}_2\} \\ \{\mathbf{U}_3\} \\ \{\mathbf{U}_4\} \end{array}}_{\text{Distribute } \tilde{\mathbf{v}}(s)} \xrightarrow{\text{Launch phase}} \underbrace{\begin{array}{l} \xrightarrow{\text{Map}} (s, \mathbf{f}_1(s), \text{Var}[\mathbf{f}_1(s)]) \\ \xrightarrow{\text{Map}} (s, \mathbf{f}_2(s), \text{Var}[\mathbf{f}_2(s)]) \\ \xrightarrow{\text{Map}} (s, \mathbf{f}_3(s), \text{Var}[\mathbf{f}_3(s)]) \\ \xrightarrow{\text{Map}} (\underbrace{s}_{\text{Key}}, \underbrace{\mathbf{f}_4(s), \text{Var}[\mathbf{f}_4(s)]}_{\text{Value}}) \end{array}}_{\text{Map Stage}} \quad (3.4)$$

$$\underbrace{\left(\begin{array}{l} \mathbf{f}_1(s), \mathbf{f}_2(s), \mathbf{f}_3(s), \mathbf{f}_4(s), \\ (s, \text{Var}[\mathbf{f}_1(s)], \text{Var}[\mathbf{f}_2(s)], \\ \text{Var}[\mathbf{f}_3(s)], \text{Var}[\mathbf{f}_4(s)]) \end{array} \right)}_{\text{Reduce Stage}} \xrightarrow{\text{Join Reduce}} (\mathbf{f}(s), \text{Var}[\mathbf{f}(s)]) \quad (3.5)$$

Our computational codes for manipulating the simulations, computing the SVD, and the matrix vector product $\mathbf{U}\tilde{\mathbf{v}}$ can be found at github.com/dgleich/simform in the branch `simform-sisc`.

4. Numerical experiment. In this section we apply the model reduction method to an uncertainty quantification (UQ) study of a large-scale heat transfer model in random heterogeneous media. In what follows, we describe the physical model, the UQ study, and the construction of the ROM. We compare the ROM’s predictions for the quantity of interest to a standard response surface approach. We close this section with some remarks on the computational issues we encountered working with four terabytes of data from the simulations.

4.1. Heat transfer model. We consider a standard partial differential equation model for heat transfer of a temperature field $T = T(x, t)$,

$$\frac{\partial}{\partial t}(\rho c_p T) = \nabla \cdot (\kappa \nabla T), \quad (x, y, z) \in \mathcal{D}, \quad t \in [0, t_f]. \quad (4.1)$$

The spatial domain \mathcal{D} is a rectangular brick of size $20 \times 10 \times 10 \text{ cm}^3$ centered at the origin.

The brick contains two materials roughly corresponding to foam ($\rho = 319 \text{ kg/m}^3$) and stainless steel ($\rho = 7900 \text{ kg/m}^3$) chosen for their contrast in thermal conductivity. The values for temperature-dependent specific heat c_p and conductivity κ are shown in Tables 7.2 and 7.1 in the appendix. The distribution of these two materials within the brick is realized by the following procedure: (i) set the material in the entire brick to steel, (ii) choose 128 locations within the brick uniformly at random, (iii) for each location, find all points in the brick within a given radius s and set the material to foam. The result is a steel brick with randomly distributed, potentially overlapping foam bubbles of radius s . The random choice of locations justifies the use of the label *random media*.

A given brick begins ($t = 0$) at room temperature $T = 298 \text{ }^\circ\text{K}$ with a Dirichlet boundary condition of $1000 \text{ }^\circ\text{K}$ on the face $x = 10 \text{ cm}$. The temperature field advances to the final time $t_f = 2000 \text{ s}$, and the quantities of interest are measured at the face opposite the prescribed boundary condition (the *far face*) at $x = -10 \text{ cm}$. We are interested in two quantities: (i) the average temperature over the far face and (ii) the proportion of the temperature on the far face that exceeds $475 \text{ }^\circ\text{K}$.

The finite element simulation is run using Sandia Labs’ SIERRA Multimechanics Module: Aria [17] with a regular mesh of $256 \times 128 \times 128$ elements constructed with CUBIT [3]. One simulation takes approximately four hours on a 8-core node of Sandia’s Red Sky capacity cluster (Dual Xeon 5500-series, 2.93 GHz, 2GB per core). The simulation outputs contain the full temperature field at nine uniformly spaced times between $t = 1200 \text{ s}$ and $t_f = 2000 \text{ s}$, which are stored in the Exodus II file format. Each simulation output file is approximately 500MB. Two representative temperature fields are shown in Figure 4.1.

4.2. UQ study. We use the heat transfer model to study the effects of the bubble radius parameter s on the temperature distribution on the far face via the quantities of interest. Intuitively, as s increases, more of the brick becomes foam, and we expect a lower temperature on the far face $x = -10 \text{ cm}$ due to foam’s lower conductivity.

To address the variability in random media, we choose 128 random realizations of the 128 locations for the bubble centers. For a given radius s , we run 128 simulations—one for each realization of the bubble locations. We use these simulations to compute Monte Carlo estimates of the mean of each quantity of interest. Note that there are 384 random variables (three components per location) characterizing the locations of the bubbles, so Monte Carlo estimates are the only feasible option.

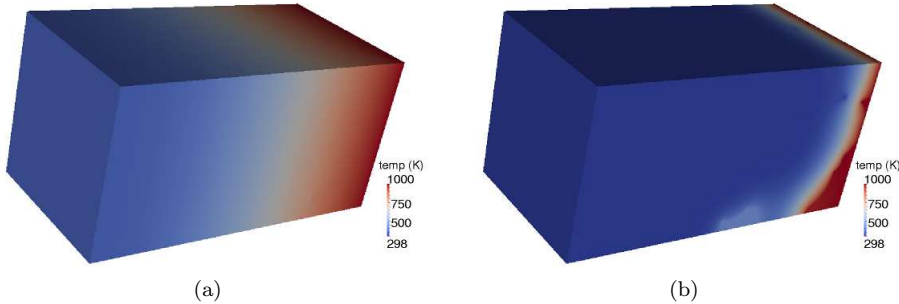


Fig. 4.1: Representative temperature fields at time $t_f = 2000$ s for bubble radius $s = 0.390$ cm (left) and $s = 2.418$ cm (right). (Colors are visible in the electronic version.)

For each realization of the bubble locations, we run 64 simulations varying s uniformly between 0.039 cm and 2.496 cm. This results in a total of 8192 simulations—128 bubble realizations \times 64 values for s . For each simulation, we compute the two quantities of interest: (i) the average temperature over the far face, and (ii) the proportion of the far face temperature that exceeds 475 °K. We then approximate the mean over the bubble realizations with Monte Carlo. Finally, we plot the estimates of the mean as a function of the radius s . Note that with 128 realizations, the 95% confidence intervals are within 1% of the mean, so we do not plot them. These results are shown in Figure 4.2. As expected, the propagation of the temperature decreases as s increases. However, the decrease is qualitatively different for the two quantities of interest: the average far face temperature decreases smoothly as a function of s while the proportion of the temperature above a threshold has a dramatic change as a function of s . In the next section, we test the ability of the reduced order model to reproduce these results.

4.3. Construction and validation of the ROM. We build the reduced order model to approximate the temperature distribution at each point in the mesh, for each of the nine points in time, and for all realizations of the bubble locations simultaneously given a value for the bubble radius. In the notation of Section 2, $f = f(x, s)$ now carries the following interpretation:

- f is the temperature,
- x contains the three spatial coordinates, the time coordinate, and an identifier for the realization of the random bubble locations,
- s is the bubble radius.

We construct the reduced order model using the simulated temperatures for bubble radii $s_j = 0.039 j$ for $j = 1, 5, 9, \dots, 61$. The matrix \mathbf{F} (see (2.6)) contains 16 columns and 4926801024 rows (257 x nodes \times 129 y nodes \times 129 z nodes \times 9 times \times 128 bubble locations), which is approximately 600 GB.

The singular values (scaled by the largest singular value) and the components of the first eight right singular vectors (scaled by their respective singular values) of \mathbf{F} are plotted in Figure 4.3. For comparison, we have included the same components from the SVD of a matrix with temperature fields for $s_j = 0.039 j$ with $j = 1, 2, 3, \dots, 64$, i.e., a matrix \mathbf{F} with 64 columns and the same roughly five billion

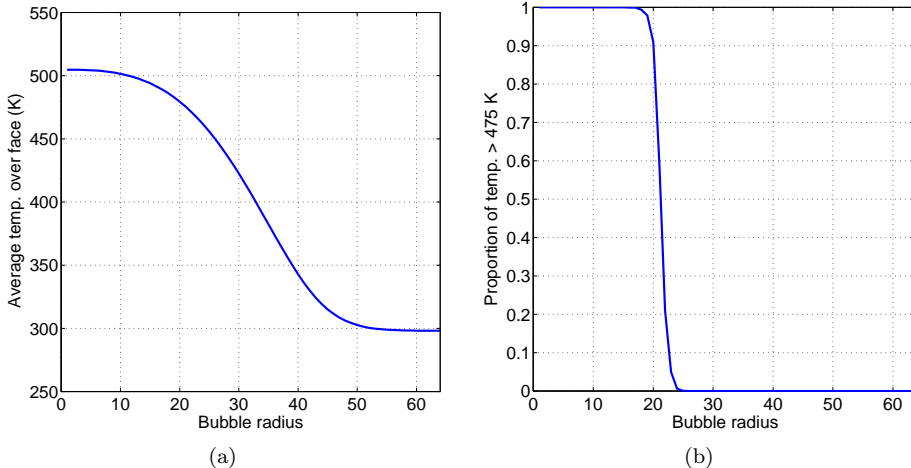


Fig. 4.2: The mean of the average far face temperature as a function of the bubble radius (left). The mean of the proportion of the temperature that exceeds 475°K as a function of the bubble radius. (Colors are visible in the electronic version.)

rows—approximately 2.2 TB of data.

We computed this SVD and all other MapReduce-based analyses of this dataset on a 10-node Hadoop cluster at Stanford University’s Institute for Computational and Mathematical Engineering. Each node in the cluster has 6 2TB hard drives, one Intel Core i7-960, and 24 GB of RAM. The 600 GB matrix took approximately 8 hours, and the 2.2TB GB matrix took approximately 12 hours. Below, we discuss the time required for additional pre- and post-processing work.

The rapid decay of the singular values in Figure 4.3b indicates the tremendous correlation amongst components of the temperature fields as the radius varies. More importantly, we see the more rapid increase in the oscillations of the right singular vectors for larger values of s . This reflects the fact that temperature fields with similar bubble radii have larger differences for larger values of the radius s . This also means we expect a more accurate ROM for smaller values of s .

To choose the threshold $\bar{\tau}$ that defines the splitting described in Section 2.4, we compute (i) the error in the ROM’s mean prediction and (ii) the variation metric τ (see (2.20)) for all 16 possible splittings at radius values $s_j = 0.039j$ with $j = 3, 7, 11, \dots, 59$, which were not used in the ROM construction. Figure 4.4 shows the errors as a function of the bubble radius s and the variation threshold $\bar{\tau}$. We see that after $\bar{\tau} = 0.55$, the approximation does not improve with more terms (i.e., larger R in (2.11)), so we choose $\bar{\tau} = 0.55$. Table 4.1 displays the splitting R and the associated error \mathcal{E} for the different values of s using variation threshold $\bar{\tau}$.

Finally, we qualitatively compare the error in the ROM to the prediction variance. Figure 4.5 displays the ROM error and the prediction variance at the final time t_f for one realization of the bubble locations and two values of the bubble radius, $s = 0.39\text{ cm}$ and $s = 1.95\text{ cm}$. Visually, the error and the prediction variance have a similar spatial distribution.

4.4. Comparison to a response surface. One question that arises frequently in the context of reduced order modeling is, if one is only interested in a scalar quantity

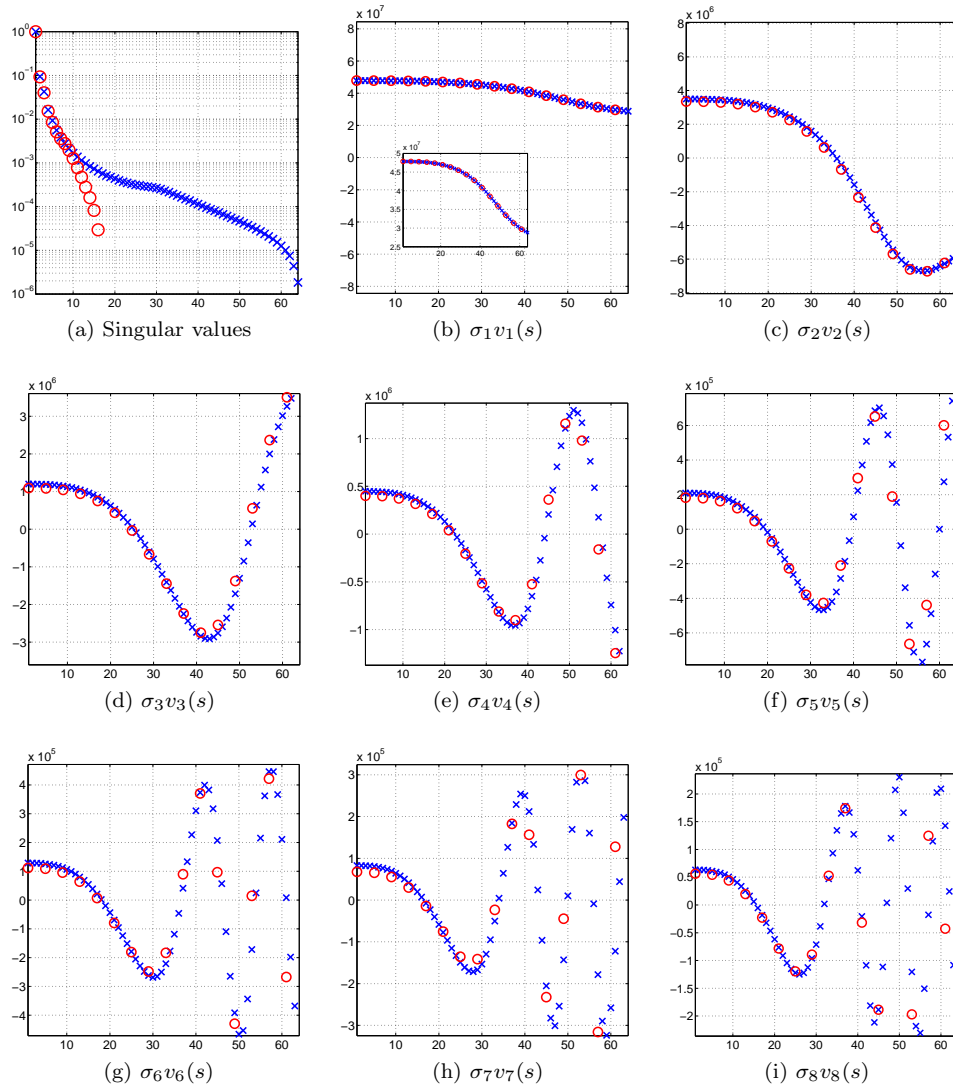


Fig. 4.3: The top left figure shows the singular values of a finely resolved \mathbf{F} with 64 columns (blue x's) and a coarsely resolved \mathbf{F} with 16 columns (red o's). Each are scaled by the maximum singular value from each set. The remaining figures show the approximations of the singular functions $v_1(s)$ through $v_8(s)$ scaled by the respective singular values for \mathbf{F} with 64 columns (blue x's) and 16 columns (red o's). (Colors are visible in the electronic version.)

of interest from the full PDE solution, then what is the advantage of approximating the full solution with a reduced order model? Why not just use a scalar response surface to approximate the quantity of interest as a function of the parameters? To address this question, we compare two approaches for the UQ study in Section 4.2:

1. Use a cubic spline response surface to interpolate the means of each of the two quantities of interest over a range of radii. The response surface is trained

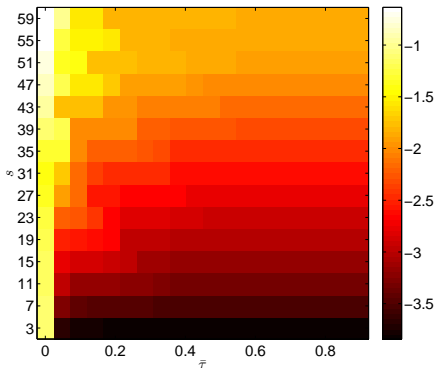


Fig. 4.4: The log of the relative error in the mean prediction of the ROM as a function of s and $\bar{\tau}$. (Colors are visible in the electronic version.)

s	$R(s, \bar{\tau})$	$\mathcal{E}(s, \bar{\tau})$
0.08	16	1.00e-04
0.23	15	2.00e-04
0.39	14	4.00e-04
0.55	13	6.00e-04
0.70	13	8.00e-04
0.86	12	1.10e-03
1.01	11	1.50e-03
1.17	10	2.10e-03
1.33	9	3.10e-03
1.48	8	4.50e-03
1.64	8	6.50e-03
1.79	7	8.20e-03
1.95	7	1.07e-02
2.11	6	1.23e-02
2.26	6	1.39e-02

Table 4.1: The split and the corresponding ROM error for $\bar{\tau} = 0.55$ and different values of s .

on the mean quantities of interest for bubble radii $s_j = 0.039j$ for $j = 1, 5, 9, \dots, 61$. The response surface prediction is then computed for $j = 1, 2, 3, \dots, 61$.

2. Use the ROM to approximate the temperature field on the far face at the final time for each realization of the bubble location. Then compute the two quantities of interest for each approximated far face temperature distribution, and compute a Monte Carlo approximation of the mean.

The results of this study are shown in Figure 4.6. For the first quantity of interest (the average temperature over the far face), the response surface approach adequately captures the behavior as a function of the bubble radius due to the relative smoothness of the response. However, the response surface approximation of the second quantity of interest (the proportion of far face temperature that exceeds 475 °K) is substantially less accurate than the ROM due to the sharp transition as the bubble radius varies. Additionally, the oscillations in the response surface near the transition admit values above 1 and below 0, which is not possible for a proportion. Note that a piecewise linear response surface would not contain such over and undershoots, but it would also fail to resolve the sharp transition beyond the resolution of $\Delta s = 4$. A global polynomial or radial basis function approximation would likely fare worse due to the global nature of the basis. We conclude that the choice of ROM versus response surface depends on the quantity of interest.

4.5. Computational considerations. We end this section with a few notes on the experience of running 8192 large scale simulations—each generating 500 MB of data, transferring them to a Hadoop cluster, and building the reduced order model.

Each heat transfer simulation took approximately four hours using eight processors on Sandia’s Red Sky. Communication times were negligible, but some runs required multiple tries due to occasional network failures. Also, some runs had to be duplicated due to node failures and changes in the code paths. Each mesh with

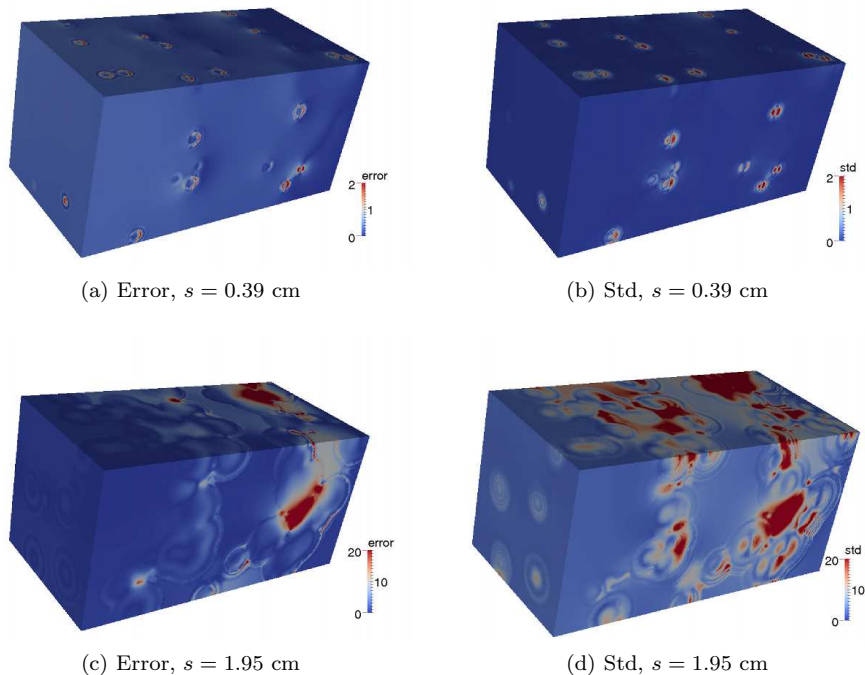


Fig. 4.5: Error in the reduce order model compared to the prediction standard deviation for one realization of the bubble locations at the final time for two values of the bubble radius, $s = 0.39$ and $s = 1.95$ cm. (Colors are visible in the electronic version.)

the varying conductivity fields took approximately twenty minutes to construct using Cubit after substantial optimizations.

Working with the simulation data involved a few pre- and post-processing steps: interpret 4TB of Exodus II files from Aria, globally transpose the data, compute the TSSVD, and compute predictions and errors. The preprocessing steps took approximately 8-15 hours. We collected precise timing information, but we do not report it as these times are from a multi-tenant, unoptimized Hadoop cluster where other jobs with sizes ranging between 100GB and 2TB of data sometimes ran concurrently. Also, during our computations, we observed failures in hard disk drives and issues causing entire nodes to fail. Given that the cluster has 40 cores, there was at most 2400 cpu-hours consumed via these calculations—compared to the 131,072 hours it took to compute 4096 heat transfer simulations on Red Sky. Thus, evaluating the ROM was about 50-times faster than computing a full simulation.

We used 20,000 reducers to convert the Exodus II simulation data. This choice determined how many map tasks each subsequent step utilized—around 33,000. We also found it advantageous to store matrices in blocks of about 16MB per record. The reduction in the data enabled us to use a laptop to compute the coefficients of the ROM and apply to the far face for the UQ study in Section 4.4.

Here are a few pertinent challenges we encountered while performing this study. Generating 8192 meshes with different material properties and running independent

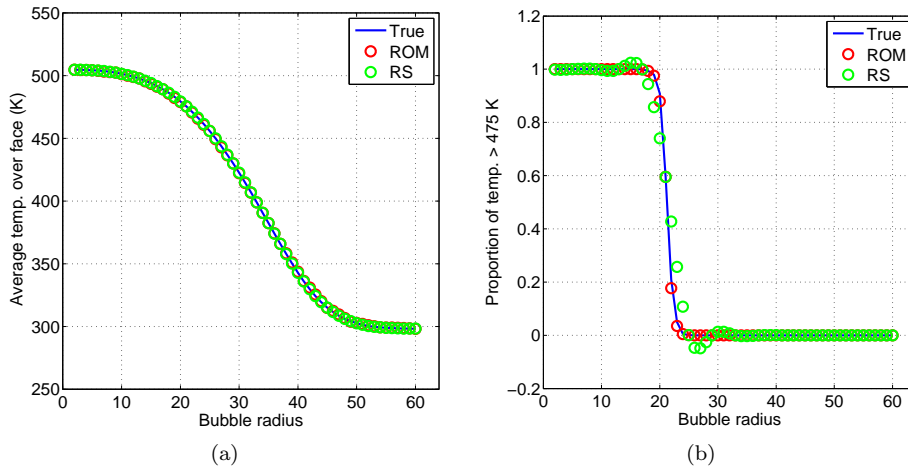


Fig. 4.6: Comparing ROM with response surface in the UQ study. (Colors are visible in the electronic version.)

simulations involved its fair share of difficulties. File system down time, error-prone communication networks, and failed runs meant that many of the simulations were submitted multiple times—and each time at the end of the queue with diminishing priority. Unreliable network data transmissions and bursty data write patterns (e.g., one hundred jobs on Red Sky simultaneously transferring data to the Stanford cluster) forced us to write custom codes to validate the data transfer. Although MapReduce is an appealing paradigm for computing factorizations of tall and skinny matrices, the Hadoop MapReduce ecosystem has not developed simple tools for working with large databases of spatiotemporal data. For instance, writing ad-hoc utilities to extract data from Exodus II files and utilities for simply stated queries like, *retrieve all values of temperature with $x = -0.1$ and $t = 2000$* , occupied much of the second and third authors' time (see the `mr-exodus2farface.py` code in the online code for this particular script). We see many high impact opportunities for software designed to address the mundane details of manipulating and analyzing large databases of spatiotemporal simulation data.

5. Summary & conclusions. We presented a non-intrusive method for building a reduced order model of the solution of a parameterized partial differential equation. The method is based on approximating the factors of a singular value expansion of the solution using the elements of a singular value decomposition of a matrix whose columns are discretized solutions at different parameter values. The SVD step is similar to reduced basis methods, which then project the governing equations with a subset of the left singular vectors to create small system whose solution yields the coefficients of the reduced order model. In contrast, our method interpolates the right singular vectors in the parameter space to compute the coefficients of the ROM—hence the label *non-intrusive*. By examining the derivative of the right singular vectors as the index increases, we determine a separation between factors we can confidently interpolate and those whose oscillations are too rapid to be represented on the parameter grid. This separation yields a mean prediction and a prediction covariance for each point in the spatio-temporal domain—similar to Gaus-

sian process regression models. We compute the SVD using a Hadoop/MapReduce implementation of the communication avoiding, tall and skinny SVD, which enables the computation to scale to outputs from large-scale high fidelity models.

We tested the model reduction method on an uncertainty quantification study of large-scale heat transfer in random media. We compared the results of the ROM to a standard response surface method for approximating the scalar quantities of interest, and we found that while the cheaper response surface was appropriate for smooth quantities of interest, the ROM was better at approximating quantities of interest with sharp transitions in the parameter space.

The 8192 heat transfer simulations used in the study generated approximately 4 TB of data. In the course of the study, we applied the MapReduce-based SVD computation to a matrices with approximately 600 GB and 2.2 TB of data. We found that existing tools for working with such large-scale simulation data lack robustness and generality. There is an opportunity in computational science to improve these tools to further simulation-based scientific exploration.

6. Acknowledgments. We thank Margot Gerritsen at Stanford’s Institute for Computational and Mathematical Engineering for procurement of and access to the Hadoop cluster. We thank Austin Benson at Stanford for his superb code development for the TSQR and TSSVD. We thank Joe Ruthruff at Sandia for his efforts developing the infrastructure to run the Aria cases. Finally, we thank David Rogers at Sandia and acknowledge the funding of Sandia’s Computer Science Applied Research (CSAR) program.

7. Appendix. The tables with material properties for foam and steel.

Foam ($\rho = 319 \text{ kg/m}^3$)		Steel ($\rho = 7900 \text{ kg/m}^3$)	
T (K)	κ (W/mK)	T (K)	κ (W/mK)
303	0.0486	273	13.4
523	0.0706	373	16.3
		773	21.8
		973	26.0

Table 7.1: Thermal conductivity κ . Linear interpolation is used between specified values. Constant values are used outside of the bounds.

Foam ($\rho = 319 \text{ kg/m}^3$)		Steel ($\rho = 7900 \text{ kg/m}^3$)	
T (K)	c_p (J/kgK)	T (K)	c_p (J/kgK)
296	1269	273	502
323	1356	673	565
373	1497		
423	1843		
473	1900		
523	2203		

Table 7.2: Specific heat capacity c_p . Linear interpolation is used between specified values. Constant values are used outside of the bounds.

REFERENCES

- [1] IVO BABUŠKA, FABIO NOBILE, AND RAÚL TEMPONE, *A stochastic collocation method for elliptic partial differential equations with random input data*, SIAM Journal on Numerical Analysis, 45 (2007), pp. 1005–1034.
- [2] AUSTIN BENSON, DAVID F. GLEICH, AND JAMES DEMMEL, *Direct tall-and-skinny QR factorizations in mapreduce architectures*, arXiv, cs.DC (2012), p. 1301.1071.
- [3] TED D BLACKER, WJ BOHNHOFF, AND TL EDWARDS, *Cubit mesh generation environment. volume 1: Users manual*, tech. report, Sandia National Labs., Albuquerque, NM (United States), 1994.
- [4] TAN BUI-THANH, KAREN WILLCOX, AND OMAR GHATTAS, *Model reduction for large-scale systems with high-dimensional parametric input space*, SIAM Journal on Scientific Computing, 30 (2008), pp. 3270–3288.
- [5] CLOUDERA, *Hadoop version 0.20.2 in cloudera hadoop distribution version cdh3u4*. <http://www.cloudera.com>, 2012.
- [6] PAUL G CONSTANTINE AND DAVID F GLEICH, *Tall and skinny qr factorizations in mapreduce architectures*, in Proceedings of the second international workshop on MapReduce and its applications, ACM, 2011, pp. 43–50.
- [7] PAUL G CONSTANTINE AND QIQI WANG, *Residual minimizing model interpolation for parameterized nonlinear dynamical systems*, SIAM Journal on Scientific Computing, 34 (2012), pp. A2118–A2144.
- [8] JEFFREY DEAN AND SANJAY GHEMAWAT, *MapReduce: Simplified data processing on large clusters*, in Proceedings of the 6th Symposium on Operating Systems Design and Implementation (OSDI2004), 2004, pp. 137–150.
- [9] JAMES DEMMEL, LAURA GRIGORI, MARK HOEMMEN, AND JULIEN LANGOU, *Communication-optimal parallel and sequential qr and lu factorizations*, SIAM Journal on Scientific Computing, 34 (2012), pp. A206–A239.
- [10] PC HANSEN, *Computation of the singular value expansion*, Computing, 40 (1988), pp. 185–199.
- [11] P. HANSEN, *Truncated singular value decomposition solutions to discrete ill-posed problems with ill-determined numerical rank*, SIAM Journal on Scientific and Statistical Computing, 11 (1990), pp. 503–518.
- [12] PER CHRISTIAN HANSEN, *Discrete inverse problems: insight and algorithms*, vol. 7, Society for Industrial and Applied Mathematics, 2010.
- [13] PER CHRISTIAN HANSEN, MISHA ELENA KILMER, AND RIKKE HØJ KJELDSEN, *Exploiting residual information in the parameter choice for discrete ill-posed problems*, BIT Numerical Mathematics, 46 (2006), pp. 41–59.
- [14] BINGSHENG HE, WENBIN FANG, QIONG LUO, NAGA K. GOVINDARAJU, AND TUYONG WANG, *Mars: a mapreduce framework on graphics processors*, in Proceedings of the 17th international conference on Parallel architectures and compilation techniques, PACT '08, New York, NY, USA, 2008, ACM, pp. 260–269.
- [15] PHILIP HOLMES, JOHN L LUMLEY, AND GAL BERKOOZ, *Turbulence, coherent structures, dynamical systems and symmetry*, Cambridge University Press, 1998.
- [16] DAISUKE MORI, YUSAKU YAMAMOTO, AND SHAO-LIANG ZHANG, *Backward error analysis of the alreduce algorithm for householder qr decomposition*, Japan Journal of Industrial and Applied Mathematics, 29 (2012), pp. 111–130.
- [17] P.K. NOTZ, S.R. SUBIA, M.M. HOPKINS, H.K. MOFFAT, AND D.R. NOBLE, *Aria 1.5: User manual*, Tech. Report SAND2007-2734, Sandia National Laboratories, Albuquerque, NM 87185 and Livermore, CA 94551, Apr. 2007.
- [18] STEVEN J. PLIMPTON AND KAREN D. DEVINE, *Mapreduce in mpi for large-scale graph algorithms*, Parallel Computing, 37 (2011), pp. 610–632.
- [19] CARL EDWARD RASMUSSEN, *Gaussian processes for machine learning*, (2006).
- [20] GIANLUIGI ROZZA, DBP HUYNH, AND ANTHONY T PATERA, *Reduced basis approximation and a posteriori error estimation for affinely parametrized elliptic coercive partial differential equations*, Archives of Computational Methods in Engineering, 15 (2008), pp. 229–275.
- [21] JUSTIN TALBOT, RICHARD M. YOO, AND CHRISTOS KOZYRAKIS, *Phoenix++: modular mapreduce for shared-memory systems*, in Proceedings of the second international workshop on MapReduce and its applications, MapReduce '11, New York, NY, USA, 2011, ACM, pp. 9–16.
- [22] VARIOUS, *Hadoop version 0.20, cloudera cdh3*. <http://hadoop.apache.org>, <http://cloudera.com>, 2010.
- [23] DONGBIN XIU AND JAN S HESTHAVEN, *High-order collocation methods for differential equations with random inputs*, SIAM Journal on Scientific Computing, 27 (2005), pp. 1118–1139.